

The Wanderer: Charting WASP-77A b’s Formation and Migration Using a System-Wide Inventory of Carbon and Oxygen Abundances

DAVID R. CORIA ¹, NEDA HEJAZI ¹, IAN J. M. CROSSFIELD,¹ AND MALEAH RHEM¹

¹*Department of Physics & Astronomy, University of Kansas, Lawrence, KS, USA*

ABSTRACT

The elemental and isotopic abundances of volatiles like carbon, oxygen, and nitrogen may trace a planet’s formation location relative to H₂O, CO₂, CO, NH₃, and N₂ “snowlines”, or the distance from the star at which these volatile elements sublimate. By comparing the C/O and ¹²C/¹³C ratios measured in giant exoplanet atmospheres to complementary measurements of their host stars, we can determine whether the planet inherited stellar abundances from formation inside the volatile snowlines, or non-stellar C/O and ¹³C enrichment characteristic of formation beyond the snowlines. To date, there are still only a handful of exoplanet systems where we can make a direct comparison of elemental and isotopic CNO abundances between an exoplanet and its host star. Here, we present a ¹²C/¹³C abundance analysis for host star WASP-77A (whose hot Jupiter’s ¹²C/¹³C abundance was recently measured). We use MARCS stellar atmosphere models and the radiative transfer code TurboSpectrum to generate synthetic stellar spectra for isotopic abundance calculations. We find a ¹²C/¹³C ratio of 51 ± 6 for WASP-77A, which is sub-solar (~ 91) but may still indicate ¹³C-enrichment in its companion planet WASP-77A b ($^{12}\text{C}/^{13}\text{C} = 26 \pm 16$, previously reported). Together with the inventory of carbon and oxygen abundances in both the host and companion planet, these chemical constraints point to WASP-77A b’s formation beyond the H₂O and CO₂ snowlines and provide chemical evidence for the planet’s migration to its current location ~ 0.024 AU from its host star.

Keywords: Planet hosting stars — Exoplanet Systems — Hot Jupiters — Exoplanet Migration — Exoplanet formation — Exoplanet atmospheric composition — Elemental abundances — Isotopic abundances

1. BACKGROUND

1.1. *Refractory Abundances and the Star-Planet Connection*

Stellar composition has long been implicated in planet formation— after all, stars and planets form out of the same disk of gas and dust albeit through different mechanisms. Different protoplanetary disk compositions and planet formation mechanisms have diverse outcomes which produce rocky terrestrial planets, super-Earths, sub-Neptunes, and even gas giants like Jupiter and Saturn. Since stellar atmospheres evolve slowly, the elemental abundances of exoplanet hosts tend to reflect the composition of their planet-forming disks (Brewer et al. 2016) and have the potential to yield constraints on planet formation processes and, in turn, even the

physical properties of exoplanets themselves (Bedell et al. 2018). One of the best known links between stellar abundances and exoplanets is stellar metallicity. The occurrence rate of close-in (<1 au) Jupiter-class planets is increased around higher metallicity stars (Valenti and Fischer 2005; Johnson 2010; Mortier et al. 2013). This relation is interpreted as support for the core accretion model: protoplanetary disks around more metal-rich stars often have higher masses and metal contents (Andrews et al. 2013) and can sustain solids for longer periods (Bitsch and Mah 2023), which allows giant planets to form more efficiently. Planet formation is therefore predicted to be unlikely in metal-poor environments lacking sufficient metals to form planetary cores and kick-start accretion (Andrews et al. 2013; Boley et al. 2021; Bitsch and Mah 2023). The relation with host-star metallicity, though weaker, has also been observed for sub-Neptunes and Super-Earths (Wang and Fischer 2015; Petigura et al. 2018; Boley et al. 2024). Besides

stellar metallicity, there is also a correlation between the abundances of individual refractory elements like (Mg, Si, Al, Ti) and planetary occurrence rates (Adibekyan et al. 2012). For example, giant-planet host stars exhibit higher refractory-to-iron abundance ratios than non-host stars. In Neptune-class planet hosts, there is notable increase in [Ti/Fe], [Si/Fe], [Al/Fe], and [Mg/Fe] compared to non-host stars.

Refractory-to-volatile ratios also become useful in tracing giant exoplanet formation and migration for the hot and ultra-hot Jupiter-class exoplanets (Hands and Helled. 2022; Lothringer et al. 2021). In these planets with equilibrium temperatures greater than 2000 K, refractory elements like Fe, Mg, and Si are not condensed, except perhaps on the night side, but rather gaseous and observable in the planet’s atmosphere (Lothringer et al. 2021). Using these atmospheric refractory-to-volatile abundance ratios, we may infer a planet’s rock-to-ice fraction and constrain planet formation and migration scenarios (Lothringer et al. 2021). Furthermore, formation of a planet beyond the water snowline followed by inward migration results in excess accretion of oxygen-poor, refractory-rich material leading to super-stellar alkali metal abundances but stellar water abundances in the planet’s atmosphere (Hands and Helled. 2022).

1.2. Volatile Element Abundances as Formation Diagnostics

Similarly, the stellar abundances of volatile elements like H, C, N, O, and S may shed light on giant exoplanet formation mechanisms, planet composition and atmospheric evolution (Bedell et al. 2018; Brewer and Fischer 2016; Fortney 2012; Delgado Mena et al. 2021; Turrini et al. 2021; Crossfield 2023). Stellar carbon and oxygen abundances are particularly important formation diagnostics because of their influence on exoplanet ice, gas, and rock chemistry. Formation mechanisms such as gravitational instability for brown dwarfs and core accretion for Jupiter-class exoplanets each leave behind unique carbon and oxygen signatures in the atmospheres of these sub-stellar objects. Formation via gravitational instability occurs more rapidly than core accretion, on sub-Myr timescales, which results in brown dwarfs with stellar to super-stellar C/O ratios and abundances characteristic of their progenitor molecular clouds, similar to binary star systems (Ilee et al. 2017; Hawkins et al. 2020). Core accretion, on the other hand, is a much slower process, occurring on Myr timescales, which allows for protoplanets to incorporate varying quantities of gas and solids into their atmospheres, potentially resulting in a wide range of atmospheric metallicities and

C/O ratios, but maintaining sub-stellar carbon and oxygen abundances (Xuan et al. 2024b).

Multiple studies also explore the possibility of using elemental abundance ratios like the carbon-to-oxygen ratio (Oberg et al. 2011; Madhusudhan et al. 2014; Mordasini et al. 2016; Ali-Dib et al. 2017; Reggiani et al. 2022; Seligman et al. 2022) to constrain a planet’s formation location relative to “snowlines”, or the distance from a star where volatile molecules like H₂O, CH₄, CO, and CO₂ condense into ice grains. When a planet forms within the H₂O and CO snowlines, like Jupiter and Saturn for example, the planet is expected to inherit the same C/O ratio as its host star. When the planet forms outside the volatile snowlines, there are two main scenarios that affect the volatile abundances of these planets: (1) the planet migrates before dissipation of the protoplanetary disk resulting in atmospheric C/O ratios < 0.5 and super-solar metallicities due to the accretion of oxygen-rich planetesimals or (2) the planet migrates after dissipation of the protoplanetary disk resulting in atmospheric C/O ratios ~ 1 and sub-solar metallicities (Oberg et al. 2011; Madhusudhan et al. 2014, 2017; Madhusudhan 2019). See also (Schneider and Bitsch 2021a,b; Bitsch et al. 2022; Pacetti et al. 2022) for an in-depth analysis on how inward drifting evaporating pebbles affect volatile abundances in exoplanet atmospheres along with a couple example giant exoplanet formation scenarios.

Though precise stellar abundances provide useful context for interpreting the atmospheric composition of their companion exoplanets (Reggiani et al. 2022, 2024), there is still a need to investigate the connection between atmospheric composition, protoplanetary disk chemistry, and planetary formation inferences (Molliere et al. 2022). After all, the chemical composition of giant planets and their atmospheres are greatly affected by the accretion of gas and solids as they form and migrate to their final locations, deviating significantly from abundances of the protoplanetary disk (Pacetti et al. 2022). Comparisons of the atmospheric abundances of exoplanets to planet formation simulations provide additional, complementary constraints on planet formation pathways. The condensation sequence of H₂O, CO₂, CH₄, and CO results in an increase of the gas phase C/O ratio with radial distance from the host star, which makes the planetary C/O ratio an ideal signature of a planet’s accretion history (Bitsch et al. 2022). Besides C/O, other volatile ratios like C/N, N/O, and S/N appear to follow monotonic trends with the extent of migration—the deviation from stellar values increases with the extent of disk-driven migration (Pacetti et al. 2022). By measuring these volatile element abundances in an exoplanet’s

atmosphere, comparing them to the host star’s abundances as well as planet formation models, we may predict how and where in the disk the planet formed and infer subsequent migration.

1.3. *Isotopologue Abundance Ratios as Formation Diagnostics*

In the era of the James Webb Space Telescope (JWST), ground-based 8m- class telescopes, upcoming 30m- class telescopes, and ultra high-resolution spectroscopy, we are suddenly sensitive to the signatures of much weaker molecular absorption lines in dwarf stars, brown dwarfs and even exoplanets. In addition to the major isotopologues of CO, CH, H₂O, NH₃, we are now detecting minor isotopologues such as ¹³C¹⁶O, ¹²C¹⁸O, ¹³CH, H₂¹⁷O, H₂¹⁸O, and ¹⁵NH₃ which allow for the measurements of ¹²C/¹³C, ¹⁴N/¹⁵N, ¹⁶O/¹⁸O, and ¹⁷O/¹⁸O isotopologue ratios. The most widely observed of the CNO isotope ratios is the ¹²C/¹³C ratio. Measurements have been made in young stellar objects (Smith et al. 2015), solar twin stars (Botelho et al. 2020; Coria et al. 2023), M dwarf stars (Crossfield et al. 2019; Xuan et al. 2024a), brown dwarfs (e.g. L dwarf 2M0355, T dwarf, 2M0415, M dwarf HD 984 B, and several others) (Zhang et al. 2021b; Costes et al. 2024; Hood et al. 2024; Xuan et al. 2024b; de Regt et al. 2024), short-orbit hot-Jupiters (e.g. WASP-77A b and HD 189733 b) (Line et al. 2021; Finnerty et al. 2024) and wide-orbit Jupiters (e.g. TYC-8998 b and VHS 1256 b) (Zhang et al. 2021a; Gandhi et al. 2023) using instruments and observatories such as VLT/CRIRES, ESO/HARPS, NASA IRTF/iSHELL, Keck/KPIC, Keck/NIRSpec, Gemini/IGRINS, and JWST/NIRSpec.

These isotopic ratios are not only useful in constraining Galactic Chemical Evolution (GCE) models (Kobayashi et al. 2020; Prantzos et al. 2018; Romano et al. 2020; Romano 2022; Coria et al. 2023), but also in understanding planet formation pathways and accretion histories (Woods and Willacy 2009; Atreya et al. 2016; Zhang et al. 2021a,b; Barrado et al. 2023). The first study investigating carbon isotope fractionation in protoplanetary disks finds that the ¹²C/¹³C ratio of a system varies with radius and height in the disk (Woods and Willacy 2009). Complementary observations and measurements of the ¹²C/¹³C ratio in solar system objects provide a hint of ¹³C-enrichment of the ice giants located beyond our Sun’s CO snowline (Woods 2009). Since then, observations of ¹²C/¹³C in protoplanetary disks have unveiled different isotopic reservoirs that may imprint their signatures in exoplanet atmospheres (Zhang et al. 2017; Nomura et al. 2023; Bergin et al. 2024; Yoshida et al. 2024). Beyond the CO

snowline at around 20 AU for sun-like stars, Bergin et al. (2024) finds one reservoir enriched in ¹²C composed mainly of methane/hydrocarbon ices and a second, ¹³C-enriched reservoir dominated by gaseous CO. Zhang et al. (2021a) instead proposes ¹³C-enriched ice, found beyond the CO snowline, as a source for observed giant planet ¹³C enrichment.

Similar to elemental carbon and oxygen abundances, different formation mechanisms also produce signature atmospheric ¹²C/¹³C ratios. The sub-Myr timescales of formation via gravitational instability result in brown dwarfs with solar to super-solar ¹²C/¹³C ratios while the longer, Myr timescales of formation via core accretion allow for protoplanets to accrete ¹³C-rich ice/gas. Although there are few planetary growth models that incorporate isotopologue ratios, this particular pattern is arising from ¹²C/¹³C ratio measurements made in brown dwarfs (e.g. L dwarf 2M0355, T dwarf, 2M0415, M dwarf HD 984 B) (Zhang et al. 2021b; Costes et al. 2024; Hood et al. 2024), and lower-mass super-Jupiters (e.g. WASP-77A b, HD 189733 b, TYC-8998 b and VHS 1256 b) (Line et al. 2021; Finnerty et al. 2024; Zhang et al. 2021a; Gandhi et al. 2023). Furthermore, the ice-gas partitioning of these carbon isotopes allows for the ¹²C/¹³C ratio to be used as a tracer of a planet’s formation location and migration. Planets forming within the CO snowline are expected to inherit the host star’s ¹²C/¹³C ratio while those forming beyond the CO snowline (20 AU) are expected to accrete ¹³C-rich ice/gas which lower the planet’s ¹²C/¹³C ratio. The formation scenarios and corresponding C/O and ¹²C/¹³C ratios outlined above assume in-situ formation. However, if there is a mismatch between a planet’s C/O ratio, ¹²C/¹³C ratio, its current location, and the host star’s C/O and ¹²C/¹³C ratio, this could be an indicator for planetary migration. Recent observations of both hot Jupiters (e.g. WASP-77A b and HD 189733 b) (Line et al. 2021; Finnerty et al. 2024) and wide-orbit, directly imaged planets (e.g. VHS 1256 b and TYC 8998-760-1 b) (Gandhi et al. 2023; Zhang et al. 2021a) reveal similar ¹³C enrichment, supporting the hypothesis that hot Jupiters likely did not form in situ.

To test how planetary ¹²C/¹³C ratios change with distance with their host stars and relative to various volatile snowlines, it is necessary to measure volatile abundances in three types of targets: (1) planets located inside the CO snowline, (2) planets located outside the CO snowline, and (3) exoplanet host stars. Jupiter-class planets are the most amenable to these system-wide abundance surveys. Short-period super-Jupiters close to their host stars (within the CO snowline) can have their C/O and ¹²C/¹³C ratios measured

using transmission spectroscopy (as in [Line et al. \(2021\)](#)) while bright super-Jupiters outside the CO snowline, like TYC-8998-760-1 b ([Zhang et al. 2021a](#)), can have their C/O and $^{12}\text{C}/^{13}\text{C}$ ratios measured using a combination of spectroscopy and direct imaging techniques ([Molliere et al. 2019](#)). Although FGK-type host stars routinely have their abundances measured using standard methods ([Brewer and Fischer 2016](#); [Bedell et al. 2018](#)), cooler mid- to late- type K and M dwarfs pose a bigger challenge due to their intrinsic faintness and overwhelming molecular absorption in their spectra. However, with high-resolution, high signal-to-noise spectra and a careful analysis we may successfully measure abundances in these stars as well ([Souto et al. 2017, 2018, 2022](#); [Hejazi et al. 2023, 2024](#)). Contemporary researchers use both the stellar and planetary abundances to model exoplanet atmospheres, to infer the structure and composition of the exoplanet’s interior, and to understand how atmospheres and interiors co-evolve over time ([Madhusudhan 2012](#); [Unterborn et al. 2014](#); [Brewer et al. 2016](#); [Unterborn et al. 2017](#); [Lincowski et al. 2018, 2019](#)).

In this paper, we focus on the complementary stellar and planetary isotopic abundances of the volatile elements: carbon and oxygen. We present the $^{12}\text{C}/^{13}\text{C}$ ratio measured in exoplanet host star WASP-77A using optical CH absorption features. We then compare archival carbon and oxygen abundances and our novel $^{12}\text{C}/^{13}\text{C}$ ratio in WASP-77A to those in its companion, the hot-Jupiter WASP-77A b. Our isotope ratio measurement corroborates previous findings from stellar and planetary elemental abundance analyses that favor formation beyond the H_2O and CO_2 snowlines, rather than an in-situ formation, for WASP-77A b.

In Section 2, we provide an overview of three previous elemental abundance analyses for the host star (WASP-77A) with data from Keck/HIRES, MPG/ESO/FEROS, and ARC/ARCES. We also summarize the constraints placed on the companion planet’s (WASP-77A b) C/O and $^{12}\text{C}/^{13}\text{C}$ abundance ratios derived from thermal emission spectroscopy. WASP-77A b is a well-studied hot Jupiter, so we include the companion’s abundance measurements using data from three facilities: Gemini/IGRINS, HST/WFC3, and JWST/NIRSpec.

Section 3 provides details on our Keck/HIRES and VLT/ESPRESSO spectra, and our methodology for determining $^{12}\text{C}/^{13}\text{C}$ for the host star WASP-77A. In Section 4, we discuss WASP-77A b’s formation scenario and the possible migration mechanisms that may have transformed a once cool-Jupiter to the hot-Jupiter we see today. Finally, in Section 5, we summarize the results of our stellar $^{12}\text{C}/^{13}\text{C}$ analysis and discuss the prospects

for measuring more complementary stellar isotopologue ratios.

2. PREVIOUS OBSERVATIONS OF THE WASP-77 SYSTEM

The WASP-77 system is a visual binary otherwise known as BD -07 436. The primary star (WASP-77 A) is a moderately bright, solar metallicity G8V star ($V_{mag} = 10.3$) and the secondary star (WASP-77 B) is a fainter K dwarf at a separation of approximately $3''$. [Maxted et al. \(2013\)](#) discovered a transiting, tidally-locked planetary mass companion (WASP-77A b) to the primary with an orbital period of 1.36 days. WASP-77A b is slightly larger than Jupiter with a mass of $1.76 \pm 0.06 M_{Jup}$ and radius of $1.21 \pm 0.02 R_{Jup}$ and rather hot with an effective temperature of 1740 K ([Maxted et al. 2013](#)). Both WASP-77 A and its companion planet are well-studied, well-characterized, and prime targets for chemical composition analyses as summarized below.

2.1. Host Star: WASP-77A High-resolution Spectroscopy with Keck/HIRES, MPG/ESO/FEROS, & ARC/ARCES

[Polanski et al. \(2022\)](#) uses high-resolution, high signal-to-noise optical spectra from Keck/HIRES and KeckSpec and a machine-learning-based tool to derive fundamental stellar parameters and abundances for 25 prime JWST target exoplanet host stars. Please refer to Table 1 for their adopted effective temperature, surface gravity, and [Fe/H]. Although they provide stellar abundances for 15 elements, here we include only the constraints placed on WASP-77A’s carbon, oxygen, and [Fe/H] abundances. They report stellar $[\text{C}/\text{H}] = -0.02 \pm 0.05$, $[\text{O}/\text{H}] = 0.06 \pm 0.07$, $\text{C}/\text{O} = 0.46 \pm 0.09$, and $[\text{Fe}/\text{H}] = +0.01 \pm 0.03$.

[Kolecki et al. \(2022\)](#) works with an MPG/ESO/FEROS spectrum ($\text{S}/\text{N} = 116$) to derive chemical abundances of elements most informative to planet formation and composition (C, N, O, Na, Mg, Si, S, K, and Fe). Here, we include only the stellar $[\text{C}/\text{H}] = -0.04 \pm 0.04$, $[\text{O}/\text{H}] = -0.04 \pm 0.04$, $\text{C}/\text{O} = 0.59 \pm 0.08$, and $[\text{Fe}/\text{H}] = -0.15 \pm 0.06$. Again please refer to Table 1 for the adopted stellar parameters. Notice that although they measure carbon and oxygen abundances consistent with solar values, they do, however, find a slightly subsolar [Fe/H].

[Reggiani et al. \(2022\)](#) also determined the effective temperature, surface gravity, and [Fe/H] for WASP-77A using an optical spectrum (from ARC/ARCES at the Apache Point Observatory), ATLAS9 model atmospheres ([Castelli and Kurucz 2003](#)), the MOOG radiative transfer code ([Snedden 1973](#); [Snedden et al. 2012](#)),

and the *isochrones* package (Morton et al. 2015). Please refer to Table 1 for their adopted stellar parameters. They infer elemental abundances for WASP-77A using the equivalent width method and find $[C/H] = 0.1 \pm 0.09$, $[O/H] = 0.23 \pm 0.02$, and $C/O = 0.44 \pm 0.07$. These abundances are mostly consistent with previous publications: Maxted et al. (2013), Kolecki et al. (2022), and Polanski et al. (2022). These abundances for WASP-77A b and its host star are indicative of formation beyond the H_2O snowline, rather than in situ. We discuss this further in Section 4.

2.2. Differences Between Abundance Measurements

The relevant stellar parameters and abundances discussed above are shown in Table 1. All three studies above find a slightly subsolar iron abundance for WASP-77A and a solar to slightly subsolar C/O ratio. Though mostly consistent, there are a few notable discrepancies in effective temperature, $[Fe/H]$, carbon and oxygen abundance values. Oxygen abundances are notoriously difficult to determine, particularly when using optical spectra where there is a shortage of detectable atomic oxygen lines with both observational and theoretical complications (Ting et al. 2018). In this case, however, the differences are likely due to the slightly different T_{eff} and $[Fe/H]$ values adopted.

Generally, significant differences in abundance measurements can be caused by a number of factors including the choice of input stellar parameters (T_{eff} , $\log g$, $[Fe/H]$), the selected stellar model atmospheres, the radiative transfer code used for generating synthetic spectra, and the preferred atomic and molecular line lists. We refer the reader to Kolecki et al. (2022) Section 5.2 and the references therein for a more detailed discussion of abundance discrepancies. For future isotopologue analyses, this means that an elemental abundance fit prior to measuring isotopic abundances is necessary to ensure the best possible fit between the base model spectrum and the observed spectrum as this is the starting point for generating the $^{12}C/^{13}C$ model grid.

2.3. WASP-77A b Thermal Emission Spectroscopy

WASP-77A b is an excellent candidate for transit spectroscopy and is actually one of the highest signal-to-noise ratio planets for thermal emission measurements in the near-infrared (Kempton et al. 2018)– making this hot Jupiter an ideal target for atmospheric characterization.

Line et al. (2021) provides secondary eclipse spectroscopy of WASP-77A b. The single 4.7 hour time-series sequence was taken with Gemini-South/IGRINS (Park et al. 2014; Mace et al. 2018) on December 14,

2020. The resulting spectrum is high-resolution ($R \sim 45,000$) with wavelength coverage spanning 1.43 - 2.42 μm .

The IGRINS analysis reports a planetary $[C/H] = -0.46_{-0.16}^{+0.17}$, $[O/H] = -0.49_{-0.12}^{+0.14}$, and a carbon-to-oxygen ratio $C/O = 0.59 \pm 0.08$. More importantly, they also retrieve a constraint on the $^{12}CO/^{13}CO$ ratio: 10.2-42.6 at 68% confidence. The sub-solar carbon and oxygen abundances in WASP-77A b suggest an atmosphere depleted in metals, at least based on extrapolation from the solar system planets. Although a comparison to solar abundances is a natural first step, the key is to make the comparison with the planet’s host star abundances. Refer to Section 4 for an abundance comparison between the host star WASP-77A and the companion planet WASP-77A b and see Table 1 for a list of all available carbon and oxygen abundances and metallicities for the WASP-77A system.

Mansfield et al. (2022) presents another set of secondary eclipse observations for WASP-77A b, this time with the Hubble Space Telescope’s WFC3 covering wavelengths 1.1-1.7 μm and Spitzer/IRAC at 3.6 and 4.5 μm . This atmospheric retrieval places a 3σ lower limit on the atmospheric H_2O abundance: $\log(n_{H_2O}) > -4.78$ but was unable to constrain the CO abundance and individual $[C/H]$ and $[O/H]$ abundances. There are no carbon-bearing molecule features resolved in this emission spectrum, which results in a poor constraint on the C/O ratio: a 2σ upper limit of $C/O = 0.78$. The retrieval’s best fit metallicity is $[M/H] = 0.43_{-0.28}^{+0.36}$. This value is much higher and less precise than that derived from the high-resolution Gemini/IGRINS observations. After performing a grid fit to a combination of the WFC3 and Spitzer data, they derive a metallicity of $[M/H] = 0.10_{-0.31}^{+0.43}$, which is more consistent with the high-resolution measurement.

Recent secondary eclipse observations of WASP-77A b with JWST/NIRSpec (August et al. 2023) cover the wavelength range 2.8-5.2 μm and contains several H_2O and CO features but no CO_2 . The atmospheric retrieval finds a sub-solar metallicity $[M/H] = -0.91_{-0.16}^{+0.24}$ and a C/O ratio = $0.36_{-0.09}^{+0.10}$ as well as molecular abundances of $\log_{10}(n_{H_2O}) = -4.26_{-0.10}^{+0.14}$ for water and $\log_{10}(n_{CO}) = -4.58_{-0.24}^{+0.27}$ for carbon monoxide. These results agree with the Gemini/IGRINS abundances from Line et al. (2021) within $\sim 1\sigma$ for $[Fe/H]$ and $\sim 1.8\sigma$ for the C/O ratio.

3. METHODS: ISOTOPE ANALYSIS

3.1. The Spectrum

We observed WASP-77A with the HIRES spectrograph (Vogt et al. 1994) at the Keck Observatory. The

582-second exposure of WASP-77A was taken on February 22, 2021 06:03 UT by the California Planet Search collaboration (Lead: Andrew Howard, Caltech). They use the C2 decker under effective seeing conditions of roughly $1.3''$. Standard reduction routines and telluric corrections are applied resulting in a spectrum of $R \sim 45,000$ and median signal-to-noise of 82. The final spectrum covers a wavelength range of $3600\text{-}4400 \text{ \AA}$. This is the same spectrum analysed in Polanski et al. (2022). Additionally, we also utilize publicly available ESO data for WASP-77A. This 14400-second exposure of WASP-77A was taken on October 29, 2021 02:03 UTC using VLT/ESPRESSO’s ultra-high-resolution (UHR) mode. The data is reduced using the ESPRESSO data-reduction software (DRS) pipeline, and the final extracted, wavelength-calibrated spectrum has $R \sim 140,000$, $S/N = 511$ and covers a wavelength range of $3770\text{-}7898 \text{ \AA}$.

3.2. Generating the Synthetic Spectra Grid

We will measure CH isotopologue abundances in WASP-77A by comparing the observed spectrum to synthetic spectra generated from custom 1D hydrostatic MARCS stellar atmosphere models (Gustafsson et al. 2008) and the LTE radiative transfer code TurboSpectrum (Version 15.1) (Plez et al. 2012). Although there is an extensive grid of MARCS models, we further used the interpolation routine developed by Thomas Masseron¹ to interpolate models with the same physical parameters as those of our target star. We also use the set of atomic and molecular line lists, assuming solar abundances from (Grevesse et al. 2007), as described in Hejazi et al. (2023). This includes atomic line data from the Vienna Atomic Line Database (VALD, Ryabchikova et al. (2015)) and molecular line lists from multiple sources including VALD for TiO, the Kurucz (Smithsonian) Atomic and Molecular Database (Kurucz et al. 1995), and the high resolution transmission molecular absorption database (HITRAN, Rothman et al. (2021)). The most important molecular bands for this study are: FeH (Dulick et al. 2003), CN (Brooke et al. 2014; Sneden et al. 2014), and CH (Masseron et al. 2014).

Initially, we adopt the effective temperature, surface gravity, and $[\text{Fe}/\text{H}]$ (as a proxy for the bulk stellar metallicity) values for WASP-77 A derived from our Keck/HIRES spectrum using the machine-learning tool KeckSpec: $T_{eff} = 5569 \pm 77 \text{ K}$, $\log g = 4.45 \pm 0.09$, and $[\text{Fe}/\text{H}] = 0.01 \pm 0.03$ (Polanski et al. 2022). At this point, we have not altered individual elemental abun-

dances from solar values. However, the base model generated from these parameters did not appear to fit the spectral lines surrounding several target ^{13}CH lines in the HIRES spectrum, particularly for atomic iron lines and molecular CH lines. The problem persists for a couple lines in the higher-quality ESPRESSO spectrum, but the overall fit is greatly improved. This leads us to believe that the issue with these specific lines lies in the opacity calculations or the atomic and molecular line lists incorporated in synthesizing spectra rather than the base stellar parameters. Rather than choose a set of effective temperature, surface gravity, and $[\text{Fe}/\text{H}]$ (as a proxy for the bulk stellar metallicity) from one particular study, we instead adopt weighted averages (weights = $1/\sigma^2$ where σ is the parameter uncertainty) for the stellar parameters since the effective temperature and surface gravity values are similar for the three previous host star studies (Polanski et al. 2022; Reggiani et al. 2022; Koleccki et al. 2022): $T_{eff} = 5545 \pm 22 \text{ K}$, $\log g = 4.45 \pm 0.02$. Please refer to Section 3.7 for further explanation of how our choice of fundamental stellar parameters affects the derived $^{12}\text{C}/^{13}\text{C}$ ratio.

From these chosen stellar parameters, we then generate a grid of synthetic spectra with $^{12}\text{C}/^{13}\text{C}$ ratios of 30, 50, 60 80, 90, 100, 110, 130, 160. These model spectra cover wavelengths $3600 - 4400 \text{ \AA}$ where there are numerous ^{12}CH and ^{13}CH lines suitable for this isotopologue abundance analysis.

3.3. Line Selection

We utilize TurboSpectrum’s built-in equivalent-width calculation feature to generate a list of equivalent widths of the ^{12}CH and ^{13}CH lines from the base model. From that list, we remove all ^{13}CH lines with $\text{EW} < 1.5 \text{ \AA}$ and are left with 95 candidate absorption lines. We narrow down this line list via a visual inspection of our base model spectrum. Lines from the final set are later accepted or rejected from the final $^{12}\text{C}/^{13}\text{C}$ calculation depending on overall model fit and continuum renormalization. Please refer to Table 2 for our final ^{13}CH line list. We also include information for atomic and molecular lines located within the renormalization window of our ^{13}CH lines of interest.

3.4. Continuum Re-normalization

After applying a Gaussian filter to smooth the model spectra to a spectral resolution $\sim 45,000$ for the HIRES spectrum and $\sim 140,000$ for the ESPRESSO spectrum, and performing an RV correction to the observed spectrum, we begin the continuum selection and renormalization following the methods described in Hejazi et al. (2023). The ^{13}CH features in the optical

¹ <https://marcs.astro.uu.se/software.php>

are significantly weaker than the ^{13}C O features identified in the M-band (4.5-5.0 μm) and so this isotopic abundance analysis demands a more precise continuum-selection and re-normalization process than in Coria et al. (2023). Otherwise, even a slight misalignment between the observed spectrum and the model grid (either wavelength or continuum normalization misalignment) makes determining the best fit model nearly impossible.

For each of the selected ^{13}CH lines, we visually inspect a 4-5 \AA window around the line center. We then carefully select the continuum/pseudocontinuum regions around the line-of-interest, making sure to exclude all other absorption features. From the selected continuum points, we perform an iterative sigma-clipping, 2σ then 1.5σ , to keep only those continuum/pseudocontinuum points with the best fit between the base model and the observed spectrum. For those remaining continuum/pseudocontinuum points, we perform a polynomial fit to the residuals $R = O/M$, where O is the observed flux and M is the interpolated model flux at each shifted, observed wavelength. Finally, we divide the observed spectrum by the polynomial fit to re-normalize and align continuum/pseudocontinuum levels of the observed spectrum to the models. See Figure 1 for an example renormalization using an isolated ^{13}CH line.

Unfortunately, even after a careful line-by-line renormalization, there are still regions of the observed spectrum that our models are not able to reproduce successfully. This may be due to spectral noise and bad pixels in the observed spectrum, insufficiencies in model assumptions and opacity calculations as well as atomic and molecular line lists incorporated in synthesizing spectra. Other factors such as NLTE effects are typically negligible in solar type stars (Nissen et al. 2018). Magnetic field effects are also negligible when measuring CNO abundances (Shchukina et al. 2016) but may result in an underestimate of iron abundances (Fabbian et al. 2012). Regardless, this means that we must remove lines from our analysis where the poor fit interferes with our ability to reliably determine the stellar $^{12}\text{C}/^{13}\text{C}$ ratio. This leaves only three candidate lines for the HIRES spectrum and five lines for the ESPRESSO spectrum where both the continuum/pseudo-continuum and nearby atomic absorption lines of the model spectra align well with that of the observed spectrum.

3.5. Statistical Significance

We remind the reader that our HIRES spectrum has a resolution $R \sim 45,000$ and a median signal-to-noise ratio of 82 over the wavelength range of 3600-4400 \AA . Although this spectrum is fairly high S/N, the ^{13}CH lines in this study are exceedingly weak. Therefore, we calcu-

late the BIC factor ($\text{BIC} = \chi^2 + n_{\text{dof}} * \ln(N_{\text{data}})$, where n_{dof} is the number of degrees of freedom = 1, and N_{data} is the number of data points used in the fit) for the selected ^{13}CH lines to test the statistical significance of our detection. We determine $\Delta\text{BIC}_{160-BF}$ (BIC between the observed spectrum and the model with $^{12}\text{C}/^{13}\text{C} = 160$ minus BIC between the observed spectrum and the best-fit $^{12}\text{C}/^{13}\text{C}$ model) for the ^{13}CH lines in Table 3. This $\Delta\text{BIC}_{160-BF}$ tells us if the observed spectrum significantly favors low ^{13}C -enrichment (or the $^{12}\text{C}/^{13}\text{C} = 160$ model) or higher ^{13}C -enrichment (or the best fit $^{12}\text{C}/^{13}\text{C}$ model). Table 3 demonstrates a clear difference in the BIC factor, for each of our selected ^{13}CH lines, for both the HIRES and ESPRESSO analysis. This means that both observed spectra favor models with solar to super-solar ^{13}C enrichment.

3.6. Deriving Individual Line $^{12}\text{C}/^{13}\text{C}$ Ratios

We measure the $^{12}\text{C}/^{13}\text{C}$ ratio in WASP-77 A following a similar process to that described in Crossfield et al. (2019); Coria et al. (2023). We calculate χ^2 between the re-normalized observed spectrum and each model spectrum, for each line over a wavelength range (typically 0.1-0.3 Angstroms) previously determined during the continuum selection process. For each set of χ^2 values, we use a cubic spline fit to interpolate the minimum χ^2 which corresponds to the best-fit $^{12}\text{C}/^{13}\text{C}$ abundance. We infer 1σ confidence intervals using the region where $\Delta\chi^2 \leq 1$ (Avni et al. 1976). This gives us an estimate of the stellar $^{12}\text{C}/^{13}\text{C}$ ratio for each selected ^{13}CH line. Figures 2 - 4 show the renormalized spectra, a zoom-in on the ^{13}CH line, the χ^2 minimization, and the derived $^{12}\text{C}/^{13}\text{C}$ ratio for our selected lines in the HIRES and ESPRESSO spectra. Table 3 contains more details on the χ^2 minimization including the χ^2 fit window, the number of points fit, the χ^2 at the minimum associated with the best fit $^{12}\text{C}/^{13}\text{C}$ ratio for each line. We obtain three individual $^{12}\text{C}/^{13}\text{C}$ from the HIRES analysis and five from the ESPRESSO analysis, respectively. These values range from $^{12}\text{C}/^{13}\text{C} = 47 - 75$. Please refer to Table 3 for the list of $^{12}\text{C}/^{13}\text{C}$ ratios and their statistical uncertainties.

3.7. Systematic Uncertainties

Prior to determining the final $^{12}\text{C}/^{13}\text{C}$ ratio for WASP-77A, we must consider the systematic uncertainties involved, particularly those associated with our choice of fundamental stellar parameters and elemental abundances. To test how the selection of fundamental stellar parameters impacts the derived $^{12}\text{C}/^{13}\text{C}$ ratios, we generate several more model grids, this time varying effective temperature, surface gravity, bulk stellar metallicity, and individual C, O, Ti, and Fe abundances. We

find that changing individual elemental abundances (of species in close proximity to selected ^{13}CH lines: $[\text{Fe}/\text{H}]$, $[\text{Ti}/\text{H}]$, $[\text{C}/\text{H}]$, $[\text{O}/\text{H}]$) over the range reported in the literature values (+0.1, -0.2 dex), hardly change the model fit and the derived $^{12}\text{C}/^{13}\text{C}$ ratios at all. However, effective temperature, surface gravity, bulk stellar metallicity do have a noticeable effect on the derived $^{12}\text{C}/^{13}\text{C}$ ratios.

To determine systematic uncertainties of the derived $^{12}\text{C}/^{13}\text{C}$ ratio due to changes in effective temperature, we vary the stellar effective temperature over span comparable various literature measurements, in steps of 25 K around our chosen value of 5545 K, while holding $\log g$ and metallicity constant. We find that this plausible range of effective temperature values produces $^{12}\text{C}/^{13}\text{C}$ ratios ranging from 90-110 for the ^{13}CH line at 4231.412 Å. However, the changes in $^{12}\text{C}/^{13}\text{C}$ due to the step change in effective temperature ($\sigma_T = 3$) are much smaller than the statistical uncertainties on our measurement of $^{12}\text{C}/^{13}\text{C}$ derived from the HIRES spectrum ($\sigma = 17$). Thus, we are not limited by the uncertainties on the stellar parameters in this case. For the ESPRESSO spectrum, where the data is much more precise, the changes in $^{12}\text{C}/^{13}\text{C}$ due to the step change in effective temperature ($\sigma_T = 4$) are larger than the statistical uncertainties on our measurement of $^{12}\text{C}/^{13}\text{C}$ ($\sigma = 1$). In this case, we are somewhat limited by uncertainties on the stellar parameters.

We repeat the process to determine systematic uncertainties of the derived $^{12}\text{C}/^{13}\text{C}$ ratio due to changes in surface gravity. We now vary the stellar surface gravity in steps of 0.05 around our chosen value of 4.45, while holding effective temperature and metallicity constant. We find systematic uncertainties in the derived $^{12}\text{C}/^{13}\text{C}$ due to the change in $\log g$ to be: $\sigma_G = 2$ for the HIRES analysis and $\sigma_G = 3$ for the ESPRESSO analysis. Again, these uncertainties limit the precision of the $^{12}\text{C}/^{13}\text{C}$ ratio derived from the higher-quality ESPRESSO spectrum, but not the HIRES spectrum.

Finally, to determine systematic uncertainties of the derived $^{12}\text{C}/^{13}\text{C}$ ratio due to changes in metallicity (Z), we deviate Z in steps of 0.1 dex. These steps are larger than the uncertainties of stellar metallicity reported in the literature (< 0.05 dex), but we did this to inspect if non-solar metallicities would better reproduce spectral lines such as Ti, Mn, and CH. So, we vary the stellar metallicity in steps of 0.1 dex around our chosen value of +0.00 dex, while holding effective temperature and $\log g$ constant. We find that this plausible range of Z values produces a much broader range of $^{12}\text{C}/^{13}\text{C}$ ratios ranging from 80-140. However, none of the reasonable Z values produce a model spectrum that significantly im-

proves the fit to nearby spectral lines such as Ti, Mn, and CH. In the ESPRESSO spectrum, the models derived using $Z = +0.00$ dex fit much better than they do the HIRES spectrum.

We find that the derived $^{12}\text{C}/^{13}\text{C}$ changes by $\sigma_Z = 7$ for the HIRES analysis and $\sigma_Z = 6$ for the ESPRESSO spectrum with each step of ± 0.1 dex in bulk metallicity Z . These σ_Z are overestimates, however, since the actual uncertainties on the stellar metallicity are less than half of our chosen step size. Therefore, we report final systematic uncertainties in the derived $^{12}\text{C}/^{13}\text{C}$ ratio due to changes in stellar metallicity as $\sigma_Z = 3.5$ for the HIRES analysis and $\sigma_Z = 3$ for the ESPRESSO analysis.

Finally, we calculate the quadrature sum of σ_T , σ_G , and σ_Z as the final systematic uncertainties in the $^{12}\text{C}/^{13}\text{C}$ ratio: $\sigma_{sys} = 5$ for the HIRES analysis and $\sigma_{sys} = 6$ for the ESPRESSO analysis.

3.8. Deriving the Stellar $^{12}\text{C}/^{13}\text{C}$ Ratio

Because the target ^{13}CH spectral lines have low statistical significance and are barely visible by eye when considered individually, we derive the final stellar $^{12}\text{C}/^{13}\text{C}$ ratio from these individual estimates collectively using both statistical uncertainties and the systematic uncertainties discussed above. We determine a final, weighted average of $^{12}\text{C}/^{13}\text{C} = 66 \pm 18$ for WASP-77 A with our HIRES spectrum analysis, and a consistent, but more precise $^{12}\text{C}/^{13}\text{C} = 51 \pm 6$ from our ESPRESSO spectrum analysis. We use the methods detailed in Barlow et al. (2004) Section 2.8, "Model 2" to calculate a weighted mean using asymmetric uncertainties.

Contrary to frequent assumptions, we do not find a solar $^{12}\text{C}/^{13}\text{C}$ ratio for WASP-77A, but rather a sub-solar and even near-ISM $^{12}\text{C}/^{13}\text{C}$ ratio (solar $^{12}\text{C}/^{13}\text{C} = 91.4 \pm 1.3$, ISM $^{12}\text{C}/^{13}\text{C} \approx 68$) (Ayres et al. 2013). Compared to its host star, WASP-77A b appears slightly enriched in ^{13}C with $^{12}\text{C}/^{13}\text{C} = 26.4 \pm 16.2$ (Line et al. 2021). We further discuss what these new abundance ratios may mean for WASP-77A b's formation in the following section.

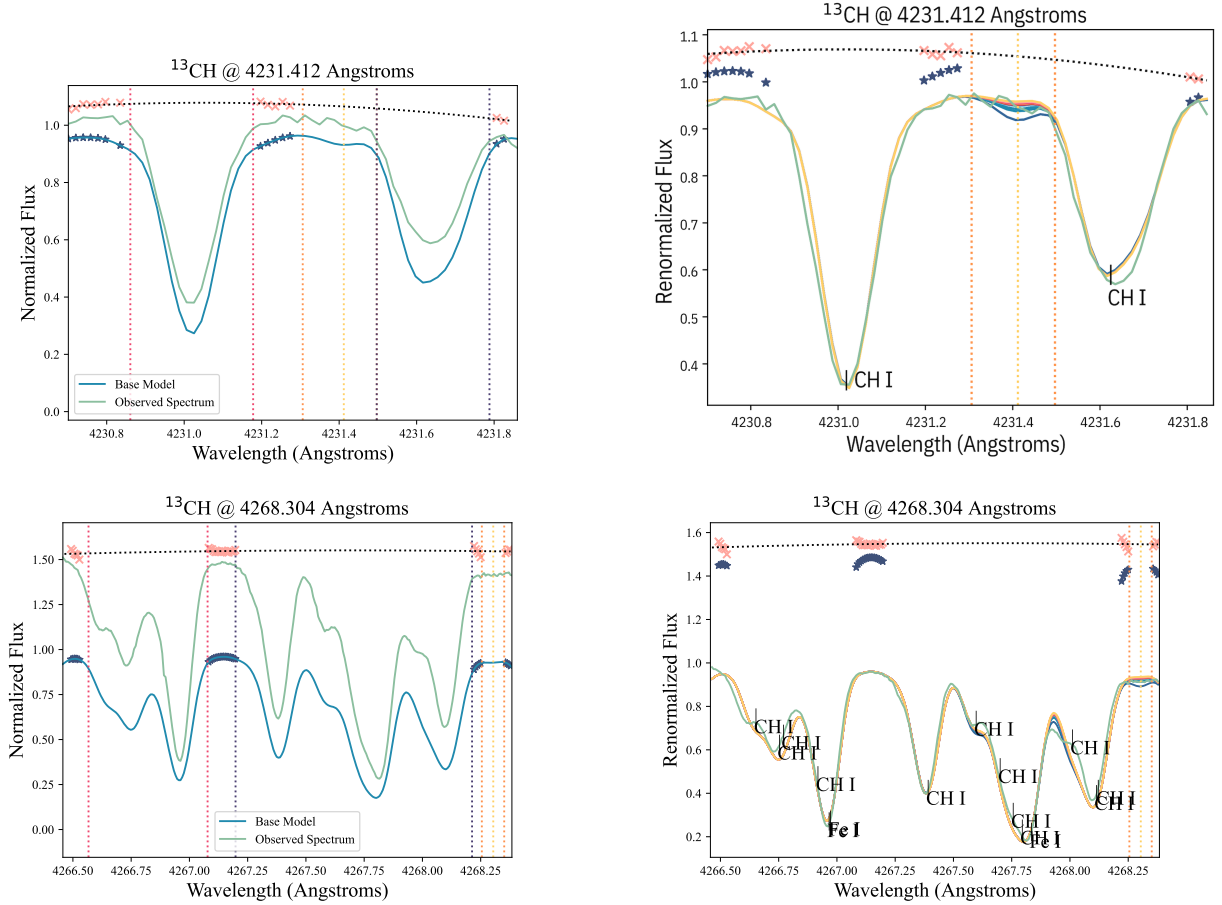


Figure 1. Pre- and post-renormalization for strong, isolated ^{13}CH lines (Top: Line at 4231.412 \AA in the HIRES spectrum; Bottom: Line at 4268.304 \AA in the ESPRESSO spectrum). The area within the orange lines shows the χ^2 fit window dominated by ^{13}CH line centered at $3982.247 \text{ Angstroms}$, while the regions covered by the red and black lines (left plot) are excluded from the continuum/pseudocontinuum selection routine. The starred points are the selected continuum/pseudocontinuum points used for renormalization. The pink points represent the residuals $R = O/M$ for the selected continuum/pseudocontinuum points and the black curve is the polynomial fit which, when divided out of the observed spectrum, provides a significantly better alignment to the target ^{13}CH line. The figures on the right highlight the location of our selected ^{13}CH lines and other nearby atomic lines.

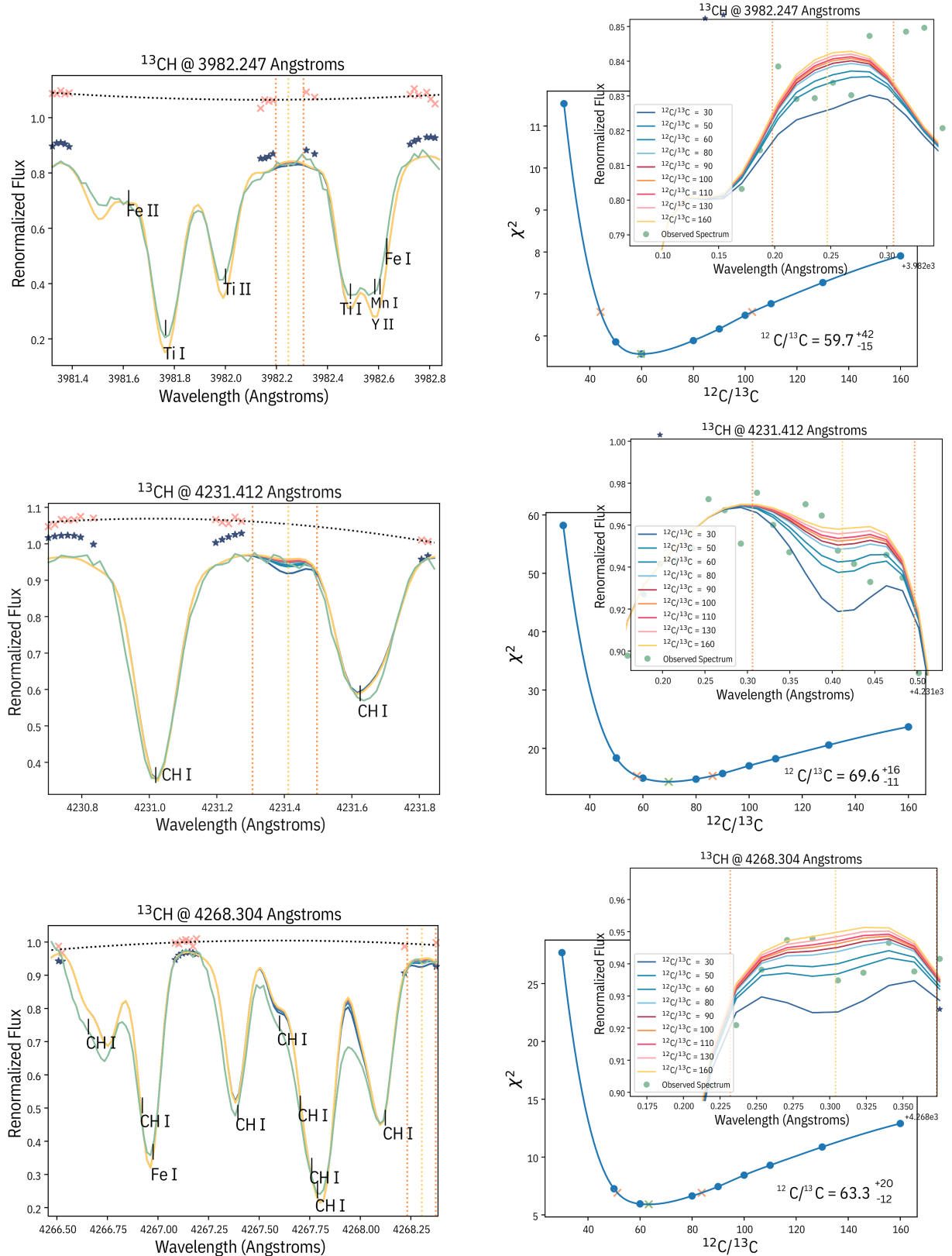


Figure 2. Interpolating the stellar $^{12}\text{C}/^{13}\text{C}$ ratio from our high-resolution and high signal-to-noise Keck/HIRES spectrum. On the left, we show our three selected ^{13}CH lines, post-normalization. We have labeled, in black, some nearby atomic and molecular lines that help us determine the best-fit base model spectrum. Refer to Table 2 for the complete line list. On the right, we zoom in on the χ^2 fit windows to better see the separation between model spectra with high and low $^{12}\text{C}/^{13}\text{C}$ ratios. We then calculate χ^2 values between the model spectra and the observed spectrum for each target line, and fit the points with a cubic spline. The minimum of the spline represents the best fit $^{12}\text{C}/^{13}\text{C}$ for the individual ^{13}CH line.

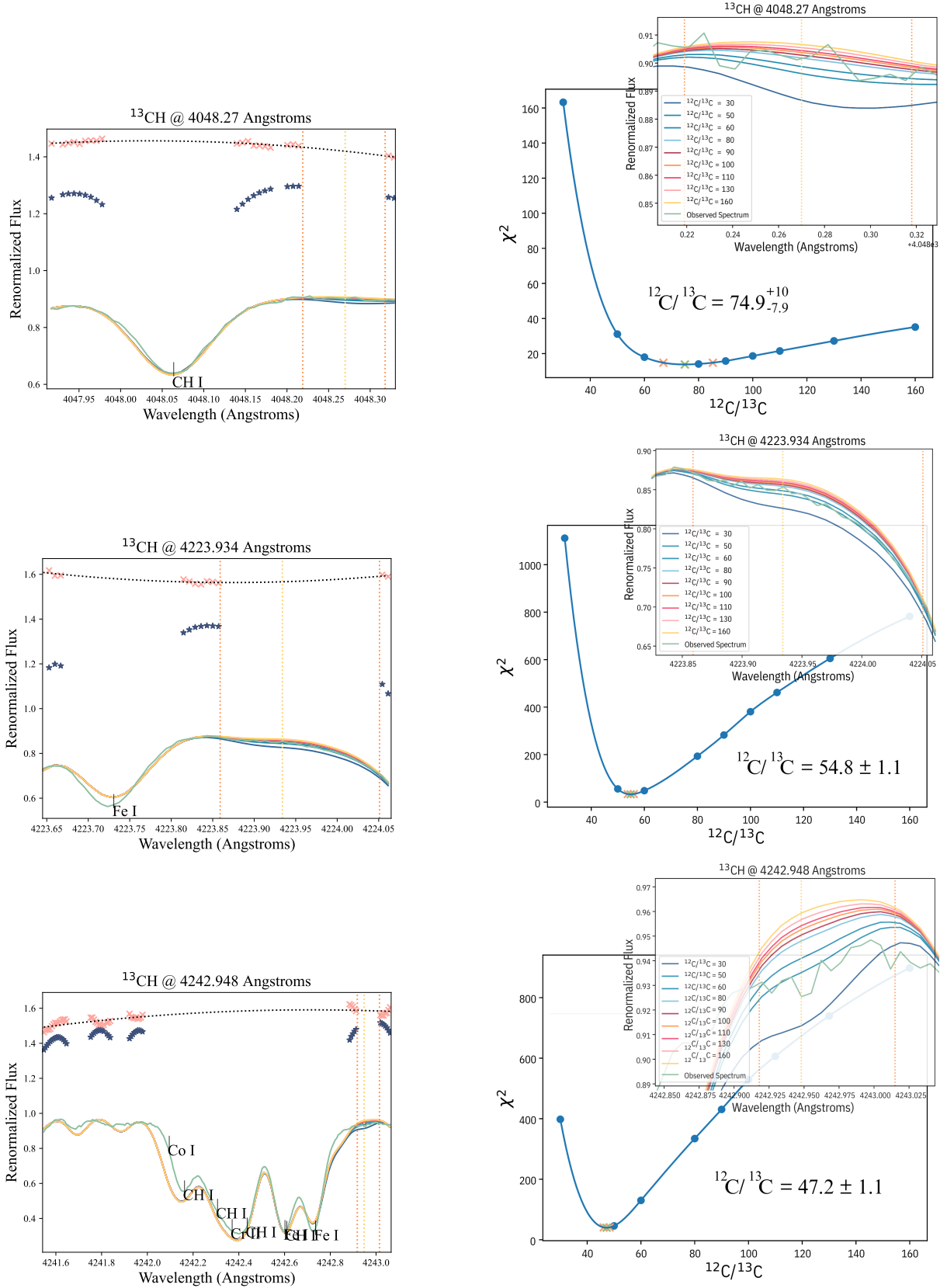


Figure 3. Interpolating the stellar $^{12}\text{C}/^{13}\text{C}$ ratio from the publicly available, high-resolution, and high signal-to-noise VLT/ESPRESSO spectrum. Similar to Figure 2, we show our selected ^{13}CH lines, post-normalization on the left. On the right, we show a zoom-in on the χ^2 fit windows and the χ^2 minimization used to determine $^{12}\text{C}/^{13}\text{C}$ for individual ^{13}CH lines.

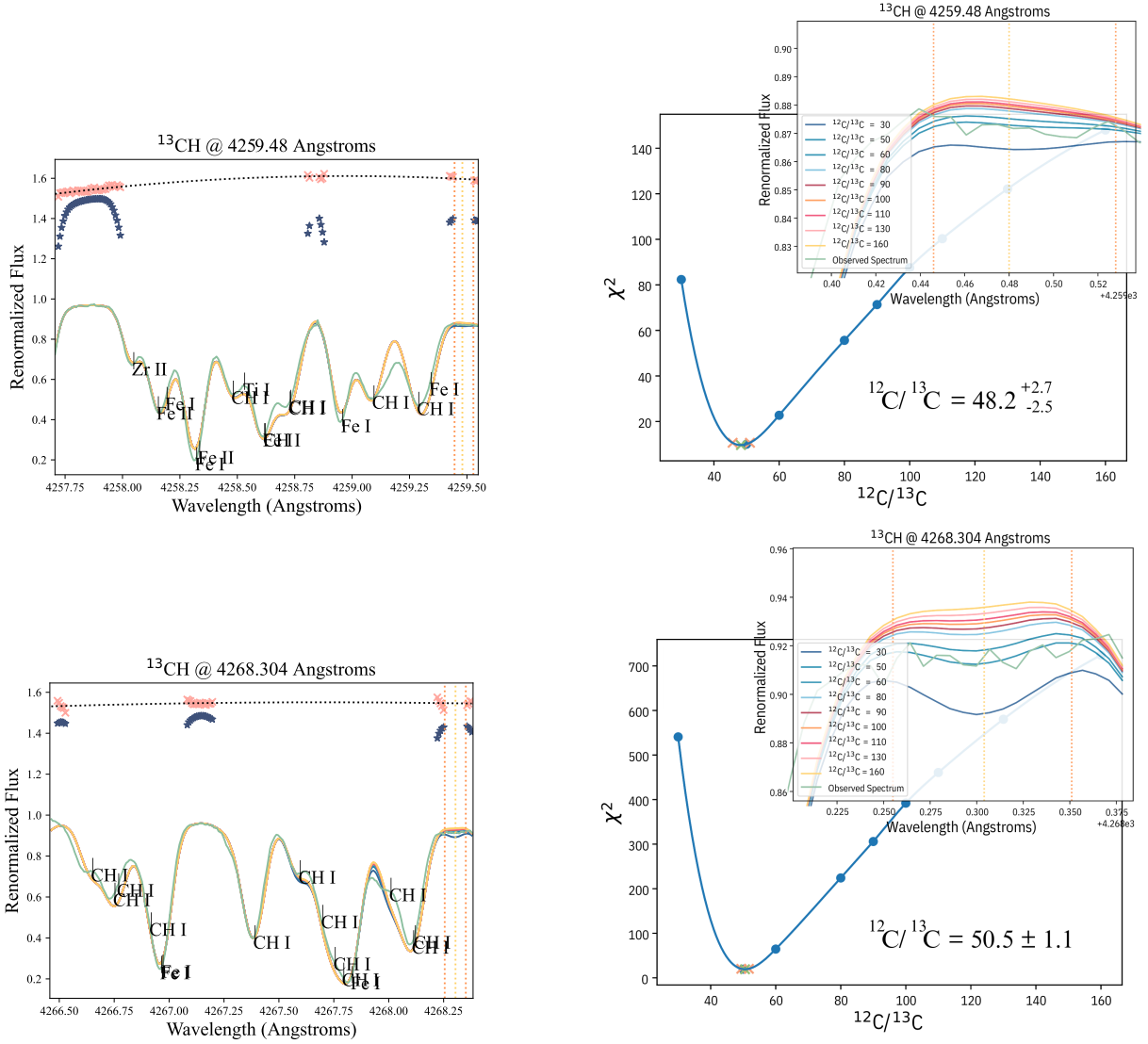


Figure 4. Interpolating the stellar $^{12}\text{C}/^{13}\text{C}$ ratio from the publicly available, high-resolution, and high signal-to-noise VLT/ESPRESSO spectrum. Similar to Figure 2, we show our selected ^{13}CH lines, post-renormalization on the left. On the right, we show a zoom-in on the χ^2 fit windows and the χ^2 minimization used to determine $^{12}\text{C}/^{13}\text{C}$ for individual ^{13}CH lines.

Table 1. WASP-77 A (Host) vs. WASP-77 Ab (Planet) Abundances

Host	Keck/HIRES	ARC/ARCES	MPG/ESO/FEROS	**Adopted
Parameter	Polanski et al. (2022)	Reggiani et al. (2022)	Kolecki et al. (2022)	Parameters
T_{eff} (K)	5569 ± 77	5525 ± 25	5660 ± 60	5545
log g	4.45 ± 0.09	4.44 ± 0.02	4.49 ± 0.03	4.45
[Fe/H]	0.01 ± 0.03	-0.05 ± 0.02	-0.15 ± 0.06	+0.00
[C/H]	-0.02 ± 0.05	0.10 ± 0.09	-0.04 ± 0.04	+0.00
[O/H]	0.06 ± 0.07	0.23 ± 0.02	-0.04 ± 0.04	+0.00
C/O	0.46 ± 0.09	0.44 ± 0.07	0.59 ± 0.08	-
Planet	Gemini/IGRINS	HST/WFC3	JWST/NIRSpec	
Parameter	Line et al. (2021)	Mansfield et al. (2022)	August et al. (2023)	
[M/H]	-0.48 ± 0.15	0.43 ± 0.36	-0.91 ± 0.24	
[C/H]	-0.46 ± 0.17	-	-	
[O/H]	-0.49 ± 0.17	-	-	
C/O	0.59 ± 0.08	< 0.78	0.36 ± 0.10	
$^{12}\text{C}/^{13}\text{C}$	26.4 ± 16.2	-	-	

NOTE—Parameters and system-wide abundance inventory for host star WASP-77A and its hot Jupiter companion WASP-77A b. **This Paper. We derive the stellar $^{12}\text{C}/^{13}\text{C}$ ratio for WASP-77A using the same HIRES spectrum as Polanski et al. (2022) and a publicly available VLT/ESPRESSO spectrum.

Table 2. Line List

Species	Line Center (Å)	Equivalent Width (Å)	Renormalization Window (Å)
¹³ CH*	3982.247	1.60	3981.321 - 3982.848
Fe I	3981.512	32.735	-
Fe II	3981.612	14.871	-
Ti I	3981.762	111.763	-
Fe I	3981.771	111.74	-
Ti II	3981.991	69.622	-
Ti I	3982.481	65.561	-
Mn I	3982.576	39.202	-
Y II	3982.592	81.178	-
Fe I	3982.624	17.647	-
¹³ CH*	4048.270	-	4047.913 - 4048.332
CH I	4048.062	30.16	-
¹³ CH*	4223.934	1.74	4223.645 - 4224.065
Fe I	4223.729	27.096	-
¹³ CH*	4231.412	1.84	4230.701 - 4231.860
Ni I	4231.032	46.739	-
Fe I	4231.597	12.83	-
CH I	4231.000	67.704	-
CH I	4231.035	69.041	-
CH I	4231.592	41.903	-
CH I	4231.680	43.164	-
¹³ CH*	4242.948	2.13	4241.542 - 4243.066
Co I	4242.089	15.963	-
Cr II	4242.364	52.167	-
Fe I	4242.595	49.534	-
Fe I	4242.729	60.709	-
CH I	4242.156	44.291	-
CH I	4242.300	46.168	-
CH I	4242.430	69.514	-
CH I	4242.603	72.165	-
¹³ CH*	4259.480	-	4257.706 - 4259.549
Zr II	4258.041	23.588	-
Fe II	4258.148	43.764	-
Fe I	4258.186	29.79	-
Fe I	4258.315	85.959	-
Fe II	4258.328	16.086	-
Ti I	4258.524	11.828	-
Fe I	4258.611	68.699	-

Table 2 *continued*

Table 2 (*continued*)

Species	Line Center (Å)	Equivalent Width (Å)	Renormalization Window (Å)
Fe I	4258.951	52.447	-
Fe I	4259.336	22.261	-
CH I	4258.474	45.463	-
CH I	4258.613	24.176	-
CH I	4258.722	48.086	-
CH I	4258.725	25.54	-
CH I	4259.087	45.468	-
CH I	4259.282	48.09	-
¹³ CH*	4268.304	2.14	4266.457 - 4268.384
Fe I	4266.958	14.204	-
Fe I	4266.964	79.921	-
Fe I	4267.826	96.387	-
CH I	4266.644	26.397	-
CH I	4266.745	25.4	-
CH I	4266.762	26.443	-
CH I	4266.910	26.815	-
CH I	4267.383	69.777	-
CH I	4267.589	25.404	-
CH I	4267.692	26.819	-
CH I	4267.748	72.441	-
CH I	4267.787	69.781	-
CH I	4268.002	30.661	-
CH I	4268.105	72.445	-
CH I	4268.113	30.14	-

NOTE—We include species, line center, and equivalent width for atomic and molecular lines within the renormalization window for each of our ¹³CH lines of interest (starred). CH line lists are from [Masseron et al. \(2014\)](#). Atomic lines are from the Vienna Atomic Line Database ([Ryabchikova et al. 2015](#)). Equivalent widths are calculated using TurboSpectrum ([Plez et al. 2012](#)). Lines without equivalent widths were identified by eye.

4. DISCUSSION

We now see slight deviations from solar abundances in WASP-77A’s photosphere. The weighted average of the three stellar abundance values from ([Polanski et al. 2022](#); [Reggiani et al. 2022](#); [Kolecki et al. 2022](#)) are $[C/H] = -0.02 \pm 0.03$, $[O/H] = 0.17 \pm 0.02$, $C/O = 0.49 \pm 0.05$, and $[Fe/H] = -0.05 \pm 0.02$. WASP-77A potentially has $[C/H]$ consistent with solar, elevated $[O/H]$, sub-solar

C/O (solar $C/O = 0.59 \pm 0.08$ ([Asplund et al. 2021](#))), and slightly sub-solar metallicity. Additionally, we now see a potential difference between the solar ¹²C/¹³C ratio (91.4 ± 1.3) and our measurement of WASP-77A’s ¹²C/¹³C ratio (51 ± 6).

Now, by comparing host star WASP-77A’s carbon, oxygen, and metallicity values to those of its hot Jupiter companion, we notice WASP-77A b’s sub-stellar $[C/H] = -0.46 \pm 0.17$, significant oxygen depletion with $[O/H] = -0.49 \pm 0.14$, $C/O = 0.50 \pm 0.06$ consistent with its host star, and sub-stellar metallicity with $[M/H] = -0.60 \pm 0.13$.

Table 3. χ^2 Minimization and Individual $^{12}\text{C}/^{13}\text{C}$ Ratios

Species	Line Center	χ^2 Fit Window	# of Points Fit	χ^2 at Minimum	$\Delta\text{BIC}_{160\text{-}Best}$	$^{12}\text{C}/^{13}\text{C}$	$^{12}\text{C}/^{13}\text{C}$
	Å	Å	H, E	H, E	H, E	H	E
^{13}CH	3982.247	3982.198 - 3982.306	7, -	5.4, -	$\Delta\text{BIC}_{160-50} = 19.775, -$	59.7^{+42}_{-15}	-
^{13}CH	4048.270	4048.219 - 4048.318	5, 15	-, 13.7	-, $\Delta\text{BIC}_{160-80} = 21.050$	-	$74.9^{+10}_{-7.9}$
^{13}CH	4223.934	4223.859 - 4224.051	11, 27	-, 32.7	-, $\Delta\text{BIC}_{160-60} = 733.981$	-	$54.8^{+1.1}_{-1.1}$
^{13}CH	4231.412	4231.306 - 4231.497	10, 21	14.6, -	$\Delta\text{BIC}_{160-100} = 6.691, -$	69.6^{+16}_{-11}	-
^{13}CH	4242.948	4242.880 - 4243.015	-, 14	-, 39.8	-, $\Delta\text{BIC}_{160-50} = 852.014$	-	$47.2^{+1.1}_{-1.0}$
^{13}CH	4259.480	4259.399 - 4259.528	7, 12	-, 9.64	-, $\Delta\text{BIC}_{160-50} = 137.960$	-	$48.2^{+2.7}_{-2.5}$
^{13}CH	4268.304	4268.232 - 4268.373	8, 14	5.9, 19.2	$\Delta\text{BIC}_{160-50} = 39.618, 704.753$	63.3^{+20}_{-12}	$50.5^{+1.1}_{-1.1}$

NOTE—The first two columns show the location of our selected ^{13}CH lines. Column 3 describes the location of the χ^2 fit window including the number data points fit (Column 4), the calculated χ^2 minimum (Column 5), and the $\Delta\text{BIC}_{160\text{-}Best}$ (Column 6) associated with the best fit $^{12}\text{C}/^{13}\text{C}$ ratios for the HIRES (H) and ESPRESSO (E) spectra (Columns 7 and 8, respectively). $\Delta\text{BIC}_{160\text{-}Best}$ is calculated as the BIC difference between the lowest ^{13}C -enriched model with $^{12}\text{C}/^{13}\text{C} = 160$, and the best-fit model.

4.1. WASP-77A b's Formation Location

Hot Jupiter systems are of particular interest for abundance studies because of their amenability for observation, but also because of their formation histories. There is only sufficient material for in-situ hot Jupiter formation in large protoplanetary disks where there are also likely to be multiple cold Jupiters in the outer disk (Batygin et al. 2016). This does not appear to be the case for WASP-77A b. Thus, we expect non-stellar abundances in hot-Jupiter atmospheres, characteristic of the planet's formation location and accretion history elsewhere in the disk. The following formation scenario for WASP-77 A b relies on the volatile abundance inventory for the WASP-77 A system (Table 1: including both host star and planetary C/H, O/H, C/O, and $^{12}\text{C}/^{13}\text{C}$ ratios) and its usage in determining formation and migration diagnostics as discussed in Sections 1.2 and 1.3.

A sub-stellar C/O ratio would indicate radial migration where the planet accumulates O-rich and C-poor material, however, WASP-77A b's C/O ratios are mostly consistent with its host star (Line et al. 2021; August et al. 2023). While the similar C/O ratios alone may be indicative of formation close to the star (within the H_2O snowline at 5 AU), it is critical to take into account individual carbon and oxygen abundances as well. The sub-stellar carbon and oxygen abundances measured in WASP-77A b's atmosphere are a signature of formation in the outer disk, beyond the H_2O and CO_2 snowlines (located at around 5 and 10 AU respectively), where most carbon and oxygen is trapped in grains, leaving the planet-feeding gas depleted in volatiles (Bosman et al. 2021). Planets forming in this outer region of the

disk are expected to have sub-stellar C/H and O/H. In fact, the sub-solar C/H, O/H, and solar C/O ratios of WASP-77A b are well reproduced by planet formation and accretion models which predict the planet's formation beyond the CO_2 evaporation front (Bitsch et al. 2022). Overall, WASP-77A b's sub-stellar atmospheric carbon and oxygen abundances and stellar C/O ratio are indicative of this planet's formation beyond the host's H_2O and CO_2 snowlines located at $\sim 5\text{AU}$ and 10 AU respectively (Oberg et al. 2011; Reggiani et al. 2022; Bitsch et al. 2022).

Though elemental abundances alone constrain WASP-77A b's formation location to be beyond both the H_2O and CO_2 snowlines, or somewhere at a separation greater than 10 AU, our goal was to make a complementary measurement of the stellar $^{12}\text{C}/^{13}\text{C}$ ratio to determine whether (1) WASP-77A b's ^{13}C enrichment was inherited from the host star, placing the formation location between the CO_2 snowline at 10 AU and the CO snowline at 20 AU or (2) whether WASP-77A b's ^{13}C enrichment was due to the accretion of ^{13}C -rich material found beyond the CO snowline at 20 AU. Our additional finding that WASP-77A has a sub-solar $^{12}\text{C}/^{13}\text{C}$ ratio of 51 ± 6 shows that the hot Jupiter WASP-77A b may indeed have ^{13}C enrichment ($^{12}\text{C}/^{13}\text{C} = 10.2\text{-}42.6$), but perhaps not as significant as when we were assuming a solar $^{12}\text{C}/^{13}\text{C}$ for the host star. Again, protoplanetary disk chemistry models produce a broad range of $^{12}\text{C}/^{13}\text{C}$ in CO as mid-plane height and radial distance from the star varies (Zhang et al. 2017; Nomura et al. 2023; Bergin et al. 2024; Yoshida et al. 2024; Line et al. 2021; Woods and Willacy 2009). Although this host star and exoplanet $^{12}\text{C}/^{13}\text{C}$ ratio comparison appears

consistent with previous studies that place WASP-77A b’s formation beyond the stellar H₂O and CO₂ snowlines located at 5 and 10 AU respectively, it is unclear whether the difference is considerable enough to suggest formation beyond the stellar CO snowline where significant ¹³C enrichment is expected occur (Zhang et al. 2021a; Bergin et al. 2024). Notably, WASP-77A b has a ¹²C/¹³C ratio inconsistent with that of any planet in our own solar system, but this is perhaps unexpected as WASP-77A b’s formation and accretion history is thought to be much different than that of our solar system planets. The ¹³C-enrichment found in WASP-77A b’s atmosphere, relative to its host star, and the elemental carbon and oxygen abundances in the system disfavor an “in situ” formation scenario nonetheless. This new piece of evidence corroborates our understanding of hot Jupiter formation from a dynamical standpoint. That is, hot-Jupiters likely did not form in situ, but rather migrated to their current positions from the outer disk. Refer to Section 4.2 for a brief dynamical explanation on how hot Jupiters form.

We emphasize that the interpretation of abundance ratios measured in giant exoplanet atmospheres relies on the abundance ratios measured in the host star’s photosphere and on planet formation and accretion models. For a further analysis of the interplay between a planet’s atmospheric carbon and oxygen abundances and different planet formation pathways in the context of the WASP-77 system, we refer the reader to Bitsch et al. (2022).

4.2. Possible Migration Mechanisms

There are several mechanisms for migration that could transform a warm/cool Jupiter into a short-period hot Jupiter. These include coplanar high-eccentricity migration (Petrovich et al. 2015b), secular chaos (Wu and Lithwick 2011), and Lidov-Kozai cycling (Wu and Murray 2003; Petrovich et al. 2015a). A recent study based on data from the California Legacy Survey (Rosenthal et al. 2021) argues that coplanar high-eccentricity migration is the most likely formation pathway for hot-Jupiter formation (Zink and Howard 2023). In this scenario, there are two cold gas giant planets that through the exchange of angular momentum and tidal interactions with the host star, culminate in a hot Jupiter. Zink and Howard (2023) finds that giant planet multiplicity is ubiquitous with an average of $1.3_{-0.6}^{+1.0}$ companions per hot Jupiter and 1.0 ± 0.3 companions per warm or cold Jupiter. This provides plenty of opportunities for hot Jupiter formation via coplanar high-eccentricity migration. Most notably, this study finds that hot Jupiter-class planets tend to have an outer companion with at

least three times its mass. In the WASP-77 system, we do not see an additional, Jupiter-class companion with mass $M > 3 M_J$ that may have driven this type of migration, but we do see a possible suspect in the secondary star, WASP-77B. This star is not well characterized, but studies find it is spectral type K5 with an effective temperature $T_{eff} = 4810 \pm 100$ K which places it a mass anywhere from 0.5-0.8 solar masses based on mass-effective-temperature relationships for stars on the main sequence (Evans et al. 2016). This is at least three times more massive than WASP-77A b, and may be the cause of the planet’s migration to its current location ~ 0.02 AU from its host star.

4.3. WASP-77B Contamination

Although we have mostly discussed the primary star WASP-77A and its, companion planet WASP-77A b, there is a third member of the system: a K dwarf star WASP-77B at a separation of approximately 3 arcseconds (Maxted et al. 2013). It could be argued that the peculiar abundances observed in WASP-77A b may be a result of chemical contamination from the secondary star WASP-77B. However, there is no clear avenue for determining elemental abundances for this star. There are only ~ 4 low signal-to-noise (Average S/N = 30) ESO/HARPS spectra of WASP-77B in the literature, no effective temperature, surface gravity, or metallicity, constraints and therefore no elemental abundances for this star in the literature. Nonetheless, such contamination seems unlikely as the seeing for our Keck/HIRES spectrum was $1.3''$ and $0.45''$ for the VLT/ESPRESSO spectrum.

5. CONCLUSIONS

5.1. Summary

Using the James Webb Space Telescope, ground-based 8m- class telescopes, and ultra high-resolution spectroscopy, we are able to characterize the composition of exoplanet atmospheres like never before. However, it is necessary to properly contextualize these atmospheric abundance constraints by comparing them to their host star’s abundances rather than to solar abundances. In the case of hot Jupiter WASP-77A b and its host star WASP-77A, metallicity, carbon, and oxygen abundances provide us an insight into the planet’s origins beyond the H₂O and CO₂ snowlines (Reggiani et al. 2022; Bitsch et al. 2022). In this paper, we derive the ¹²C/¹³C ratio for WASP-77A to complement a similar measurement in WASP-77A b made by Line et al. (2021). The sub-solar and near-ISM ¹²C/¹³C ratio we find for WASP-77A (51 ± 6) provides additional evidence for WASP-77A b’s formation beyond the H₂O and CO₂ snowlines.

5.2. Prospects for Measuring Nitrogen and Oxygen Isotopologue Ratios in Cool Dwarf Stars

With the advent of some astounding exoplanet abundance constraints (Line et al. 2021; Finnerty et al. 2024; Zhang et al. 2021a; Gandhi et al. 2023), we must continue building the catalogue of elemental and isotopic host star abundances as in Souto et al. (2017, 2018); Crossfield et al. (2019); Hejazi et al. (2023); Coria et al. (2023); Hejazi et al. (2024) with an emphasis on carbon, nitrogen, and oxygen. Stellar $[N/H]$ and $^{14}N/^{15}N$ abundances are best measured using optical CN (Snedden et al. 2014; Ryabchikova et al. 2022) and possibly NH lines. While $[C/H]$ and $^{12}C/^{13}C$ may be measured using optical CH lines as we do here, they are preferentially measured for cooler K and M dwarfs in the near-infrared using CO isotopologue lines (Goorvitch 1994; Gordon et al. 2017). In the near-infrared, we may also derive $[O/H]$, $^{16}O/^{18}O$, and possibly $^{17}O/^{18}O$ using CO, OH and H_2O isotopologue lines (Goorvitch 1994; Goldman 1982; Barber et al. 2006; Xuan et al. 2024a).

5.3. CNO Abundances in Brown Dwarfs

Besides exoplanets, brown dwarf abundances also play an important role in understanding planet formation. Y dwarfs specifically are cool enough that we may see absorption from molecules that dissociate in the atmospheres of short period hot-Jupiters and wide-orbit young Jupiters. Recent studies are able to measure $^{12}C/^{13}C$ (Lew et al. 2024; Hood et al. 2024; Costes et al. 2024), $^{14}N/^{15}N$ (Barber et al. 2006), and $^{16}O/^{18}O$ (Zhang et al. 2021b) in the atmospheres of cool brown dwarfs like 2M0355, WISE J1828, and 2M0415. CNO isotopologue ratios may provide chemical distinctions between brown dwarfs and super-Jupiters, or top-down vs. bottom-up formation models, as we start seeing ISM- or greater isotopologue ratios in brown dwarfs, but sub-stellar and sub-ISM isotopologue ratios in the super-Jupiters.

5.4. CNO Abundances in the Context of Other Planetary Systems

Jupiter-class exoplanets and their host stars provide the most practical systems with which to test how carbon, oxygen, and their respective isotopic abundance ratios change with radial distance from the host star. Specifically, the most amenable planetary systems to complementary abundance analyses are those in the WASP (Wide Angle Search for Planets) catalog (Pol-

lacco et al. 2006) and the young, wide separation, directly imaged Jupiter-class planet systems. These planetary systems are routinely targeted by JWST and ground-based observatories for transmission and emission spectroscopy and provide the best avenue for the direct comparison of stellar and planetary carbon and oxygen abundances, both elemental and isotopic. These complementary abundance surveys do, however, come with several challenges exemplified by the WASP-121 and TYC 8998-760-1 systems. WASP-121 and its ultra-hot Jupiter companion WASP-121 b (Delrez et al. 2016) are well studied both in transmission and secondary eclipse observations (Mikal-Evans et al. 2018, 2019; Kovacs et al. 2019; Sing et al. 2019). Though these observations may retrieve carbon and oxygen abundance constraints for the companion planet, complementary host star measurements are made much more difficult (and isotopic abundance measurements, impossible) by the star’s fast rotation. The recently discovered TYC-8998-760-1 is a young, K2IV star host to two wide-separation Jupiter-class planets (Bohn et al. 2020). As ESO/SPHERE direct imaging and spectroscopy prioritize observations of the planets (Zhang et al. 2021b), the chemical composition of the host star remains obscure. Furthermore, the strong magnetic fields prevalent in these young stars make it difficult to model their spectra and determine fundamental effective temperature, surface gravity, and metallicity values—let alone elemental abundances—without some significant processing of the stellar spectrum (Lopez-Valdivia et al. 2021). More work must be done to identify planetary systems where we may determine carbon, oxygen, and their respective isotopic abundances in both the host star and companion planet.

The authors of this work would like to thank the California Planet Search team for providing the HIRES spectrum (originally analyzed in Polanski et al. (2022)) that was used in this analysis. We also thank the referee for an excellent discussion on the statistical significance of our measurements and the systematic uncertainties associated with our choice of model parameters which both greatly improved this paper. Finally, the authors would also like to acknowledge the support of National Science Foundation grant AST-2108686 and NASA ICAR grant A21-0406-S003.

Facilities: W. M. Keck Observatory

REFERENCES

- Adibekyan, V. Z., Sousa, S. G., Santos, N. C., et al. 2012, *A&A*, 545, A32, doi: 10.1051/0004-6361/201219401
- Ali-Dib, M. 2017, *MNRAS*, 467, 2845, doi: 10.1093/mnras/stx260

- Andrews, S. M., Rosenfeld, K. A., Kraus, A. L., and Wilner, D. J. 2013, *ApJ*, 771, 129, doi: 10.1088/0004-637X/771/2/129
- Asplund, M., Amarsi, A. M., and Grevesse, N. 2021, *A&A*, 653, A141, doi: 10.1051/0004-6361/202140445
- Atreya, S. K., Crida, A., Guillot, T., et al. 2016, arXiv e-prints, arXiv:1606.04510, doi: 10.48550/arXiv.1606.04510
- August, P. C., Bean, J. L., Zhang, M., et al. 2023, *ApJL*, <https://arxiv.org/abs/2305.07753>
- Avni, Y. 1976, *ApJ*, 210, 642, doi: 10.1086/154870
- Ayres, T. R., Lyons, J. R., Ludwig, H.-G., Caffau, E., and Wedemeyer-Bohm, S. 2013, *ApJ*, 765, 46, doi: 10.1088/0004-637x/765/1/46
- Barber, R. J., Tennyson, J., Harris, G. J., and Tolchenov, R. N. 2006, *MNRAS*, 368, 1087, doi: 10.1111/j.1365-2966.2006.10184.x
- Barlow, R. 2004, *Asymmetric Errors*, <https://arxiv.org/abs/physics/0401042>
- Barrado, D., Mollière, P., Patapis, P., et al. 2023, *Nature*, 624, 263, doi: 10.1038/s41586-023-06813-y
- Batygin, K., Bodenheimer, P. H., and Laughlin, G. P. 2016, *ApJ*, 829, 114, doi: 10.3847/0004-637X/829/2/114
- Bedell, M., Bean, J. L., Meléndez, J., et al. 2018, *ApJ*, 865, 68, doi: 10.3847/1538-4357/aad908
- Bergin, E. A., Bosman, A., Teague, R., et al. 2024, arXiv, arXiv:2403.09739, doi: 10.48550/arXiv.2403.09739
- Bitsch, B., and Mah, J. 2023, *A&A*, 679, A11, doi: 10.1051/0004-6361/202347419
- Bitsch, B., Schneider, A. D., and Kreidberg, L. 2022, *A&A*, 665, A138, doi: 10.1051/0004-6361/202243345
- Bohn, A. J., Kenworthy, M. A., Ginski, C., et al. 2020, *ApJL*, 898, L16, doi: 10.3847/2041-8213/aba27e
- Boley, K. M., Wang, J., Zinn, J. C., et al. 2021, *AJ*, 162, 85, doi: 10.3847/1538-3881/ac0e2d
- Boley, K. M., Christiansen, J. L., Zink, J., et al. 2024, arXiv e-prints, arXiv:2407.13821, doi: 10.48550/arXiv.2407.13821
- Bosman, A. D., Alarcón, F., Bergin, E. A., et al. 2021, *ApJS*, 257, 7, doi: 10.3847/1538-4365/ac1435
- Botelho, R. B., Milone, A. d. C., Meléndez, J., et al. 2020, *MNRAS*, 499, 2196, doi: 10.1093/mnras/staa2917
- Brewer, J. M., and Fischer, D. A. 2016, *ApJ*, 831, 20, doi: 10.3847/0004-637X/831/1/20
- Brewer, J. M., Fischer, D. A., Valenti, J. A., and Piskunov, N. 2016, *ApJS*, 225, 32, doi: 10.3847/0067-0049/225/2/32
- Brooke, J. S. A., Ram, R. S., Western, C. M., et al. 2014, *ApJS*, 210, 23, doi: 10.1088/0067-0049/210/2/23
- Castelli, F., and Kurucz, R. L. 2003, *Modelling of Stellar Atmospheres*, ed. N. Piskunov, W. W. Weiss, and D. F. Gray, Vol. 210, A20, doi: 10.48550/arXiv.astro-ph/0405087
- Coria, D. R., Crossfield, I. J. M., Lothringer, J., et al. 2023, *ApJ*, 954, 121, doi: 10.3847/1538-4357/acea5f
- Costes, J. C., Xuan, J. W., Vigan, A., et al. 2024, <https://arxiv.org/abs/2404.11523>
- Crossfield, I. J. M. 2023, *ApJL*, 952, L18, doi: 10.3847/2041-8213/ace35f
- Crossfield, I. J. M., Lothringer, J. D., Flores, B., et al. 2019, *ApJL*, 871, L3, doi: 10.3847/2041-8213/aaf9b6
- de Regt, S., Gandhi, S., Snellen, I. A. G., et al. 2024, arXiv e-prints, arXiv:2405.10841, doi: 10.48550/arXiv.2405.10841
- Delgado Mena, E., Adibekyan, V., Santos, N. C., et al. 2021, *A&A*, 655, A99, doi: 10.1051/0004-6361/202141588
- Delrez, L., Santerne, A., Almenara, J. M., et al. 2016, *MNRAS*, 458, 4025, doi: 10.1093/mnras/stw522
- Dulick, M., Bauschlicher, C. W., J., Burrows, A., et al. 2003, *ApJ*, 594, 651, doi: 10.1086/376791
- Evans, D. F., Southworth, J., Maxted, P. F. L., et al. 2016, *A&A*, 589, A58, doi: 10.1051/0004-6361/201527970
- Evans, T. M., Sing, D. K., Goyal, J. M., et al. 2018, *AJ*, 156, 283, doi: 10.3847/1538-3881/aaebff
- Fabbian, D., Moreno-Insertis, F., Khomenko, E., and Nordlund, A. 2012, *A&A*, 548, A35, doi: 10.1051/0004-6361/201219335
- Finnerty, L., Xuan, J. W., Xin, Y., et al. 2024, *AJ*, 167, 43, doi: 10.3847/1538-3881/ad1180
- Fortney, J. J. 2012, *ApJL*, 747, L27, doi: 10.1088/2041-8205/747/2/L27
- Gandhi, S., de Regt, S., Snellen, I., et al. 2023, *ApJL*, 957, L36, doi: 10.3847/2041-8213/ad07e2
- Goldman, A. 1982, *Appl. Opt.*, 21, 2100, doi: 10.1364/AO.21.002100
- Goorvitch, D. 1994, *ApJS*, 95, 535, doi: 10.1086/192110
- Gordon, I. E., Rothman, L. S., Hill, C., et al. 2017, *Journal of Quantitative Spectroscopy and Radiative Transfer*, 203, 3, doi: <https://doi.org/10.1016/j.jqsrt.2017.06.038>
- Grevesse, N., Asplund, M., and Sauval, A. J. 2007, *SSRv*, 130, 105, doi: 10.1007/s11214-007-9173-7
- Gustafsson, Edvardsson, B., Eriksson, K., et al. 2008, *A&A*, 486, 951, doi: 10.1051/0004-6361:200809724
- Hands, T. O., and Helled, R. 2022, *MNRAS*, 509, 894, doi: 10.1093/mnras/stab2967
- Hawkins, K., Lucey, M., Ting, Y.-S., et al. 2020, *MNRAS*, 492, 1164, doi: 10.1093/mnras/stz3132
- Hejazi, N., Crossfield, I. J. M., Nordlander, T., et al. 2023, *ApJ*, 949, 79, doi: 10.3847/1538-4357/accb97

- Hejazi, N., Crossfield, I. J. M., Souto, D., et al. 2024, arXiv e-prints, arXiv:2407.07869, doi: 10.48550/arXiv.2407.07869
- Hood, C. E., Mukherjee, S., Fortney, J. J., et al. 2024, arXiv e-prints, arXiv:2402.05345, doi: 10.48550/arXiv.2402.05345
- Ilee, J. D., Forgan, D. H., Evans, M. G., et al. 2017, MNRAS, 472, 189, doi: 10.1093/mnras/stx1966
- Johnson, E. M. 2010, PhD thesis, University of Oregon
- Kempton, E. M.-R., Bean, J. L., Louie, D. R., et al. 2018, ASP, 130, 114401, doi: 10.1088/1538-3873/aadf6f
- Kobayashi, C., Karakas, A. I., and Lugaro, M. 2020, arXiv, doi: 10.48550/ARXIV.2008.04660
- Kolecki, J. R., and Wang, J. 2022, The Astronomical Journal, 164, 87, doi: 10.3847/1538-3881/ac7de3
- Kovacs, G., and Kovacs, T. 2019, A&A, 625, A80, doi: 10.1051/0004-6361/201834325
- Kurucz, R. L. 1995, ASP, Vol. 78, Astrophysical Applications of Powerful New Databases, ed. S. J. Adelman and W. L. Wiese, 205
- Lew, B. W. P., Roellig, T., Batalha, N. E., et al. 2024, arXiv e-prints, arXiv:2402.05900, doi: 10.48550/arXiv.2402.05900
- Lincowski, A. P., Lustig-Yaeger, J., and Meadows, V. S. 2019, AJ, 158, 26, doi: 10.3847/1538-3881/ab2385
- Lincowski, A. P., Meadows, V. S., Crisp, D., et al. 2018, ApJ, 867, 76, doi: 10.3847/1538-4357/aae36a
- Line, M. R., Brogi, M., Bean, J. L., et al. 2021, Nature, 598, 580, doi: 10.1038/s41586-021-03912-6
- Lopez-Valdivia, R., Sokal, K. R., Mace, G. N., et al. 2021, ApJ, 921, 53, doi: 10.3847/1538-4357/ac1a7b
- Lothringer, J. D., Rustamkulov, Z., Sing, D. K., et al. 2021, ApJ, 914, 12, doi: 10.3847/1538-4357/abf8a9
- Mace, G., Sokal, K., Lee, J.-J., et al. 2018, SPIE, Vol. 10702, Ground-based and Airborne Instrumentation for Astronomy VII, ed. C. J. Evans, L. Simard, and H. Takami, 107020Q, doi: 10.1117/12.2312345
- Madhusudhan, N. 2012, The Astrophysical Journal, 758, 36, doi: 10.1088/0004-637x/758/1/36
- Madhusudhan, N. 2019, A&A, 57, 617, doi: 10.1146/annurev-astro-081817-051846
- Madhusudhan, N., Amin, M. A., and Kennedy, G. M. 2014, ApJL, 794, L12, doi: 10.1088/2041-8205/794/1/L12
- Madhusudhan, N., Bitsch, B., Johansen, A., and Eriksson, L. 2017, MNRAS, 469, 4102, doi: 10.1093/mnras/stx1139
- Mansfield, M., Wisner, L., Stevenson, K. B., et al. 2022, AJ, 163, 261, doi: 10.3847/1538-3881/ac658f
- Masseron, T., Plez, B., Van Eck, S., et al. 2014, A&A, 571, A47, doi: 10.1051/0004-6361/201423956
- Maxted, P. F. L., Anderson, D. R., Collier Cameron, A., et al. 2013, PASP, 125, 48, doi: 10.1086/669231
- Mikal-Evans, T., Sing, D. K., Goyal, J. M., et al. 2019, MNRAS, 488, 2222, doi: 10.1093/mnras/stz1753
- Mikal-Evans, T., Sing, D. K., Goyal, J. M., et al. 2018, AJ, 156, 6, 283, doi: 10.3847/1538-3881/aaebff
- Molliere, P., Molyarova, T., Bitsch, B., et al. 2022, ApJ, 934, 74, doi: 10.3847/1538-4357/ac6a56
- Molliere, P., and Snellen, I. A. G. 2019, A&A, 622, A139, doi: 10.1051/0004-6361/201834169
- Mordasini, C., van Boekel, R., Molliere, P., Henning, T., and Benneke, B. 2016, ApJ, 832, 41, doi: 10.3847/0004-637X/832/1/41
- Mortier, A., Santos, N. C., Sousa, S., et al. 2013, A&A, 551, A112, doi: 10.1051/0004-6361/201220707
- Morton, T. D. 2015, isochrones: Stellar model grid package, Astrophysics Source Code Library, record ascl:1503.010
- Nissen, P. E., and Gustafsson, B. 2018, A&A Rv, 26, 6, doi: 10.1007/s00159-018-0111-3
- Nomura, H., Furuya, K., Cordiner, M. A., et al. 2023, ASP, Vol. 534, Protostars and Planets VII, ed. S. Inutsuka, Y. Aikawa, T. Muto, K. Tomida, and M. Tamura, 1075
- Oberg, K. I., Murray-Clay, R., and Bergin, E. A. 2011, AJ, 743, L16, doi: 10.1088/2041-8205/743/1/L16
- Pacetti, E., Turrini, D., Schisano, E., et al. 2022, ApJ, 937, 36, doi: 10.3847/1538-4357/ac8b11
- Park, C., Jaffe, D. T., Yuk, I.-S., et al. 2014, SPIE, Vol. 9147, Ground-based and Airborne Instrumentation for Astronomy V, ed. S. K. Ramsay, I. S. McLean, and H. Takami, 91471D, doi: 10.1117/12.2056431
- Petigura, E. A., Marcy, G. W., Winn, J. N., et al. 2018, AJ, 155, 89, doi: 10.3847/1538-3881/aaa54c
- Petrovich, C. 2015a, ApJ, 805, 75, doi: 10.1088/0004-637X/805/1/75
- Petrovich, C. 2015b, ApJ, 799, 27, doi: 10.1088/0004-637X/799/1/27
- Plez, B. 2012, Turbospectrum: Code for spectral synthesis, Astrophysics Source Code Library, record ascl:1205.004
- Polanski, A. S., Crossfield, I. J. M., Howard, A. W., Isaacson, H., and Rice, M. 2022, <https://arxiv.org/abs/2207.13662>
- Pollacco, D. L., Skillen, I., Collier Cameron, A., et al. 2006, PASP, 118, 1407, doi: 10.1086/508556
- Prantzos, N., Abia, C., Limongi, M., Chieffi, A., and Cristallo, S. 2018, MNRAS, 476, 3432, doi: 10.1093/mnras/sty316
- Reggiani, H., Galarza, J. Y., Schlaufman, K. C., et al. 2024, AJ, 167, 45, doi: 10.3847/1538-3881/ad0f93

- Reggiani, H., Schlaufman, K. C., Healy, B. F., Lothringer, J. D., and Sing, D. K. 2022, *AJ*, 163, 159, doi: 10.3847/1538-3881/ac4d9f
- Romano, D. 2022, *The Astronomy and Astrophysics Review*, 30, doi: 10.1007/s00159-022-00144-z
- Romano, D., Franchini, M., Grisoni, V., et al. 2020, *A&A*, 639, A37, doi: 10.1051/0004-6361/202037972
- Rosenthal, L. J., Fulton, B. J., Hirsch, L. A., et al. 2021, *ApJS*, 255, 8, doi: 10.3847/1538-4365/abe23c
- Rothman, L. S. 2021, *Nature Reviews Physics*, 3, 302, doi: 10.1038/s42254-021-00309-2
- Ryabchikova, T., Piskunov, N., Kurucz, R. L., et al. 2015, *PhyS*, 90, 054005, doi: 10.1088/0031-8949/90/5/054005
- Ryabchikova, T., Piskunov, N., and Pakhomov, Y. 2022, *Atoms*, 10, doi: 10.3390/atoms10040103
- Schneider, A. D., and Bitsch, B. 2021a, *A&A*, 654, A71, doi: 10.1051/0004-6361/202039640
- Schneider, A. D., and Bitsch, B. 2021b, *A&A*, 654, A72, doi: 10.1051/0004-6361/202141096
- Seligman, D. Z., Rogers, L. A., Cabot, S. H. C., et al. 2022, *PSJ*, 3, 150, doi: 10.3847/PSJ/ac75b5
- Shchukina, N., Sukhorukov, A., and Trujillo Bueno, J. 2016, *A&A*, 586, A145, doi: 10.1051/0004-6361/201526452
- Sing, D. K., Lavvas, P., Ballester, G. E., et al. 2019, *AJ*, 158, 91, doi: 10.3847/1538-3881/ab2986
- Smith, R. L., Pontoppidan, K. M., Young, E. D., and Morris, M. R. 2015, *ApJ*, 813, 120, doi: 10.1088/0004-637x/813/2/120
- Snedden, C., Bean, J., Ivans, I., Lucatello, S., and Sobeck, J. 2012, MOOG: LTE line analysis and spectrum synthesis, *Astrophysics Source Code Library*, record ascl:1202.009
- Snedden, C., Lucatello, S., Ram, R. S., Brooke, J. S. A., and Bernath, P. 2014, *ApJS*, 214, 26, doi: 10.1088/0067-0049/214/2/26
- Snedden, C. A. 1973, PhD thesis, University of Texas, Austin
- Souto, D., Cunha, K., Garc´ıa-Hern´andez, D. A., et al. 2017, *ApJ*, 835, 239, doi: 10.3847/1538-4357/835/2/239
- Souto, D., Unterborn, C. T., Smith, V. V., et al. 2018, *ApJL*, 860, L15, doi: 10.3847/2041-8213/aac896
- Souto, D., Cunha, K., Smith, V. V., et al. 2022, *ApJ*, 927, 123, doi: 10.3847/1538-4357/ac4891
- Ting, Y.-S., Conroy, C., Rix, H.-W., and Asplund, M. 2018, *ApJ*, 860, 159, doi: 10.3847/1538-4357/aac6c9
- Turrini, D., Schisano, E., Fonte, S., et al. 2021, *ApJ*, 909, 40, doi: 10.3847/1538-4357/abd6e5
- Unterborn, C. T., Hull, S. D., Stixrude, L. P., et al. 2017, arXiv, <https://arxiv.org/abs/1706.10282>
- Unterborn, C. T., Kabbes, J. E., Pigott, J. S., Reaman, D. M., and Panero, W. R. 2014, *ApJ*, 793, 124, doi: 10.1088/0004-637x/793/2/124
- Valenti, J. A., and Fischer, D. A. 2005, in *Protostars and Planets V Posters*, 8592
- Vogt, S. S., Allen, S. L., Bigelow, B. C., et al. 1994, *SPIE*, Vol. 2198, *Instrumentation in Astronomy VIII*, ed. D. L. Crawford and E. R. Craine, 362, doi: 10.1117/12.176725
- Wang, J., and Fischer, D. A. 2015, *AJ*, 149, 14, doi: 10.1088/0004-6256/149/1/14
- Woods, P. M. 2009, arXiv e-prints, arXiv:0901.4513, doi: 10.48550/arXiv.0901.4513
- Woods, P. M., and Willacy, K. 2009, *ApJ*, 693, 1360, doi: 10.1088/0004-637X/693/2/1360
- Wu, Y., and Lithwick, Y. 2011, *ApJ*, 735, 109, doi: 10.1088/0004-637X/735/2/109
- Wu, Y., and Murray, N. 2003, *ApJ*, 589, 605, doi: 10.1086/374598
- Xuan, J. W., Wang, J., Finnerty, L., et al. 2024, *ApJ*, 962, 10, doi: 10.3847/1538-4357/ad1243
- Xuan, J. W., Hsu, C.-C., Finnerty, L., et al. 2024, arXiv e-prints, arXiv:2405.13128, doi: 10.48550/arXiv.2405.13128
- Yoshida, T. C., Nomura, H., Furuya, K., et al. 2024, arXiv e-prints, arXiv:2403.00626, doi: 10.48550/arXiv.2403.00626
- Zhang, K., Bergin, E. A., Blake, G. A., Cleeves, L. I., and Schwarz, K. R. 2017, *Nature Astronomy*, 1, 0130, doi: 10.1038/s41550-017-0130
- Zhang, Y., Snellen, I. A. G., and Molliere, P. 2021a, *Astronomy and Astrophysics*, 656, A76, doi: 10.1051/0004-6361/202141502
- Zhang, Y., Snellen, I. A. G., Bohn, A. J., et al. 2021b, *Nature*, 595, 370, doi: 10.1038/s41586-021-03616-x
- Zink, J. K., and Howard, A. W. 2023, *ApJL*, 956, L29, doi: 10.3847/2041-8213/acfdab